Polar Research

Seismic and radar investigations of Fourcade Glacier on King George Island, Antarctica

Ki Young Kim,[1] Joohan Lee,[2] Myung Ho Hong,[2] Jong Kuk Hong,[2] Young Keun Jin[2] & Howong Shon[3]

1 Department of Geophysics, Kangwon National University, Chunchon 200-701, Korea
2 Korea Polar Research Institute, PO Box 32, Incheon 406-840, Korea
3 Department of Civil, Environmental and Railroad Engineering, Pai Chai University, Daejon 302-735, Korea

Keywords
Bulk density; cold/warm ice interfaces; elastic properties; fracture; seismic; radar.

Correspondence
Ki Young Kim, Department of Geophysics, Kangwon National University, Chunchon 200-701, Korea. E-mail: kykim@kangwon.ac.kr

doi:10.1111/j.1751-8369.2010.00174.x

Abstract

To determine P- and S-wave velocities, elastic properties and subglacial topography of the polythermal Fourcade Glacier, surface seismic and radar surveys were conducted along a 470-m profile in November 2006. P- and S-wave velocity structures were determined by travel-time tomography and inversion of Rayleigh wave dispersion curves, respectively. The average P- and S-wave velocities of ice are 3466 and 1839 m s^{-1}, respectively. Radar velocities were obtained by migration velocity analysis of 112 diffraction events. An estimate of 920 kg m^{-3} for the bulk density of wet ice corresponds to water contents of 5.1 and 3.2%, which were derived from the average P-wave and radar velocities, respectively. Using this density and the average P- and S-wave velocities, we estimate that the corresponding incompressibility and rigidity of the ice are 6.925 and 3.119 GPa, respectively. Synergistic interpretation of the radar profile and P- and S-wave velocities indicates the presence of a fracture zone above a subglacial high. Here, the P- and S-wave velocities are approximately 5 and 3% less than in the ice above a subglacial valley, respectively. The S-wave velocities indicate that warmer and less rigid ice underlies 10–15 m of colder ice near the surface of the glacier. Such layering is characteristic of polythermal glaciers. As a relatively simple non-invasive approach, integration of P-wave tomography, Rayleigh wave inversion and ground-towed radar is effective for various glaciological studies, including the elastic properties of englacial and subglacial materials, cold/warm ice interfaces, topography of a glacier bed and location of fracture zones.

A glacier's configuration and the density, elastic parameters, water content and temperature of the ice are useful in the analysis of glacier dynamics. As glaciologists monitor glaciers carefully for the effects of climate change, they will be aware that the previously mentioned factors vary both spatially and temporally within a glacier. Accordingly, detailed measurements within the body of a glacier are desired. Direct measurements of the physical properties of ice cores only provide on-the-spot data. As dense sampling at the surface and/or in boreholes is costly and time consuming, geophysical methods are often employed to derive nearly continuous estimates of elastic constants and water content in two or three dimensions.

S-wave velocities depend on the shear modulus (or rigidity) and density of the propagating medium; whereas P-wave velocities depend on the bulk modulus of incompressibility, shear modulus and density. The elastic parameters are thus derived from estimates of the density and seismic velocities. Since the pioneering work of Poisson (1828), many seismologists have investigated shear-wave propagation. Although several viable S-wave sources have recently been developed, most of these generate low-energy waves. The velocity anisotropy of shear waves in layered media has also limited the development of practical applications of surveys using S-waves (Danbom & Domenico 1986). Alternatively, vertically polarized S-wave (SV wave) velocities can be derived by the inversion of Rayleigh wave dispersion curves (Dorman & Ewing 1962; Aki & Richard 1980). Rayleigh waves, generated by the interaction of P- and S-waves at the surface of the Earth, are elliptically polarized in the vertical plane containing the direction of propagation.

Because the elastic constants change with depth, these surface waves exhibit dispersion in which velocity varies with wavelength or frequency (Sheriff 2002). For a horizontally layered model, phase velocities of Rayleigh waves are functions of the density and P- and S-wave velocities of each layer. Among these parameters, S-wave velocity is the dominant factor (Xia et al. 1999).

The volume and distribution of liquid water have a strong influence on ice rheology (Duval 1977). Surface melting particularly affects the rate of sliding in many glaciers (Fountain & Walder 1998; Zwally et al. 2002). Because of the relatively large dielectric constant of liquid water, the water content in temperate ice can be estimated using the observed velocity of electromagnetic waves in ice (Murray et al. 2007; Bradford & Harper 2005; West et al. 2007). Therefore, to characterize the water content of glaciers, radio echo sounding (RES) techniques have been used extensively.

King George Island (KGI) is the largest of the South Shetland Islands (SSIs) at the northern tip of the Antarctic Peninsula (Fig. 1), where a significant warming trend has been observed (King 1994; Smith et al. 1996). Much of the ice in the SSI glaciers is at or near the pressure melting point (Bintanja 1995). On KGI, the mean annual air temperature was –2.8°C for the period of 1947–1995 (Ferron et al. 2004). During 18 years from 1988 to 2005, the average rate of temperature rise at the King Sejong station on KGI was +0.03°C per year (Jeon & Suh 2006). Earlier measurements of the equilibrium line altitude (ELA) at Admiralty Bay, KGI, were less than 100 m (Curl 1980), but the ELA increased to 300–350 m within a period of two decades (Simões et al. 1999). European remote sensing satellite synthetic aperture radar (ERS SAR) imagery during the 1990s indicated that firn line elevations ranged between 160 and 270 m on KGI (Braun & Rau 2000).

The investigation site in the south-western part of KGI is 180–200 m high, and lies on an ablation surface of the polythermal Fourcade Glacier where the ELA is 270 m, which is 10 m below the ELA previously estimated in this area by the accumulation-area ratio and the ablation–accumulation balance ratio methods (Furbish & Andrews 1984). Using differential synthetic aperture radar interferometry (DInSAR), with a tandem pair of measurements on 23 and 24 October 1995, Moll et al. (2006) determined that the surface ice velocity in the western Fourcade Glacier was a few centimetres per day.

To determine the P- and S-wave velocities of the ice in the western part of the Fourcade Glacier and underlying rocks on KGI, inversions of first-arrival P-wave travel times and Rayleigh wave dispersion curves were applied, respectively. In addition, diffraction hyperbolas in ground-penetrating radar (GPR) data were analysed to get an average radar velocity that was used to estimate water content and bulk density of the ice. In this paper we will describe the field acquisition parameters, data processing and velocity estimation of P, S and radar waves using tomography, dispersion curves and hyperbolic diffractions, respectively. The depth-migrated profile of ground-towed radar reflection data, the seismic velocities, and derived elastic parameters of the ice and glacier bed will then be interpreted.

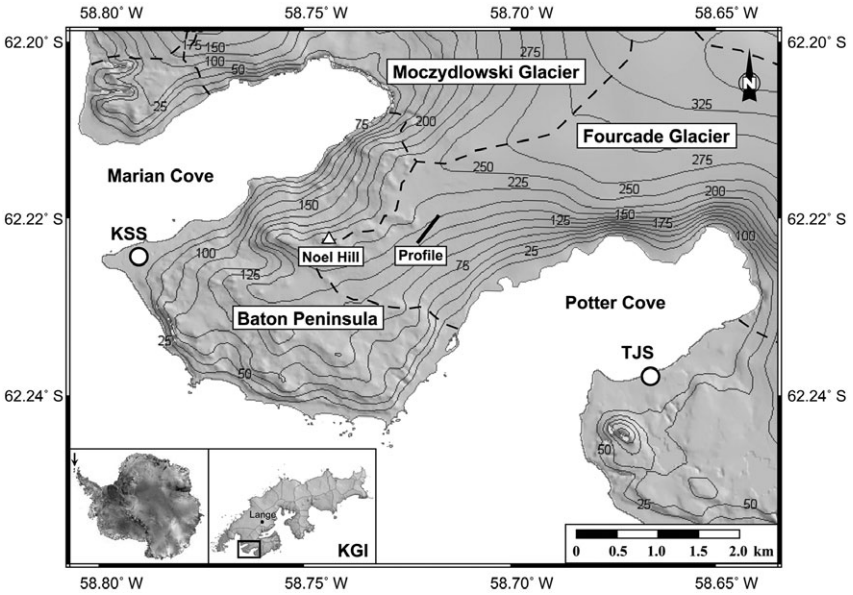

Fig. 1 Map of the western Fourcade Glacier showing the location of the 470-m seismic and radar profile, Korea's King Sejong station (KSS) Agentina's Teniente Jubany station (TJS) (modified from the satellite image map by Braun et al. 2004). Dashed lines indicate the catchment boundaries. Bare land of the Baton Peninsula bounds portions of the catchment areas of the Moczydlowski and Fourcade glaciers. The inset map of King George Island (KGI) shows the location of the "Lange" ice core recovered by Simões et al. (2004).

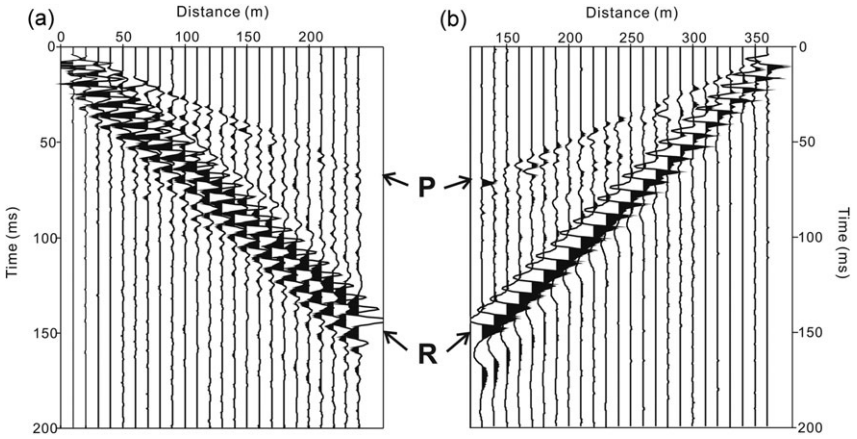

Fig. 2 Raw shot-gathered data of shot points at (a) a profile distance of 0 m, where the glacier bed is shallow, and (b) a profile distance of 370 m, where the ice is relatively thick. Relatively high S/N ratios of P waves (P) and distinct dispersion features of Rayleigh waves (R) are evident on both records.

Data acquisition

In late November 2006 we recorded both refraction and surface-wave seismic data, and GPR data, along a 470-m profile on the Fourcade Glacier of KGI, Antarctica (Fig. 1). The profile, approximately 1 km from the terminus of the glacier on Potter Cove, is roughly perpendicular to the maximum slope of the ice surface. It extends north-eastwards from the vicinity of outcrops of lapilli tuff in the Palaeocene Sejong Formation (Lee et al. 2002). Station locations and relative elevations were measured at 10-m intervals using a laser surveying instrument with a distance resolution of 3 mm km^{-1}. Locations of the profile ends were determined with a portable GPS unit. The maximum difference in elevation along the profile was less than 30 m. The thin snow cover, of several centimetres, and the isolated and relatively smooth ice field were favourable to obtaining high signal-to-noise ratios in the seismic records (Fig. 2).

Holes of 0.2–0.3 m depth were punched through the snow using a sledgehammer and a steel pipe with one end crimped to form a point. A seisgun source then fired a single 56 mm long 20-mm blank cartridge into each hole. We packed snow around the base of the seisgun in an attempt to lessen airwave noise in some cases. A total of 24 4.5-Hz vertical geophones were spaced at 10-m intervals in each geophone spread, and seven or eight shots were fired within and beyond each geophone spread using near-trace offsets of 5–20 m. The geophone spread was then moved forwards along the direction of profiling by half of the spread length, and the sequence of successive shots was repeated until the end of the profile was reached. Except at a single location, the shot holes were not reused to shoot into different geophone spreads. The data were recorded using a 24-channel McSeis-SX engineering seismograph (Oyo Corporation, Tsukuba, Japan) with a dynamic range of 108 dB. We used one geophone per channel, a record length of 1024 ms and a sampling interval of 0.5 ms. Shot gathers at 0 and 370 m show relatively high S/N ratios of first arrivals and distinct dispersion features of Rayleigh waves (Fig. 2).

To record the ground-towed GPR data (Fig. 3a), we used a RAMAC/GPR control unit full-range system and a 50-MHz cable-type unshielded antenna (Malå Geoscience, Malå, Sweden). Assuming a constant velocity of 168 m μs^{-1} in ice (Glen & Paren 1975) the vertical resolution, based on the quarter-wavelength criterion, is approximately 0.8 m, and the radius of the first Fresnel zone at 50 m depth is approximately 4.6 m for the antenna. The radar antenna had a fixed transmitter–receiver distance of 4.0 m. It generated 20-ns radar pulses, which were recorded at a temporal sampling frequency of 504 MHz. At a walking speed of 2.6 m s^{-1}, a horizontal sample rate of 7.7 traces per metre was obtained with a four-fold vertical stack.

Data processing

The ground-towed radar data were processed to get higher vertical resolution, propagation velocities and a clear depth image (Fig. 4a). The recorded seismic data were processed in two separate flows to get both the P-wave velocities (V_P) using the travel-time tomography method (Fig. 4b), and the composite image of multiple one-dimensional (1D) S-wave velocities (V_S), by inverting Rayleigh wave dispersion curves (Fig. 4c). Using both V_P and V_S, and assuming reasonable density values (ρ) deduced from the radar velocities, the bulk modulii (k) and shear modulii (μ) for the ice body and the glacier bed were computed for an isotropic model in which velocities do not vary with the direction of seismic wave propagation.

GPR data processing

Pre-processing steps for the radar data included determination of location and elevation for each trace, trace

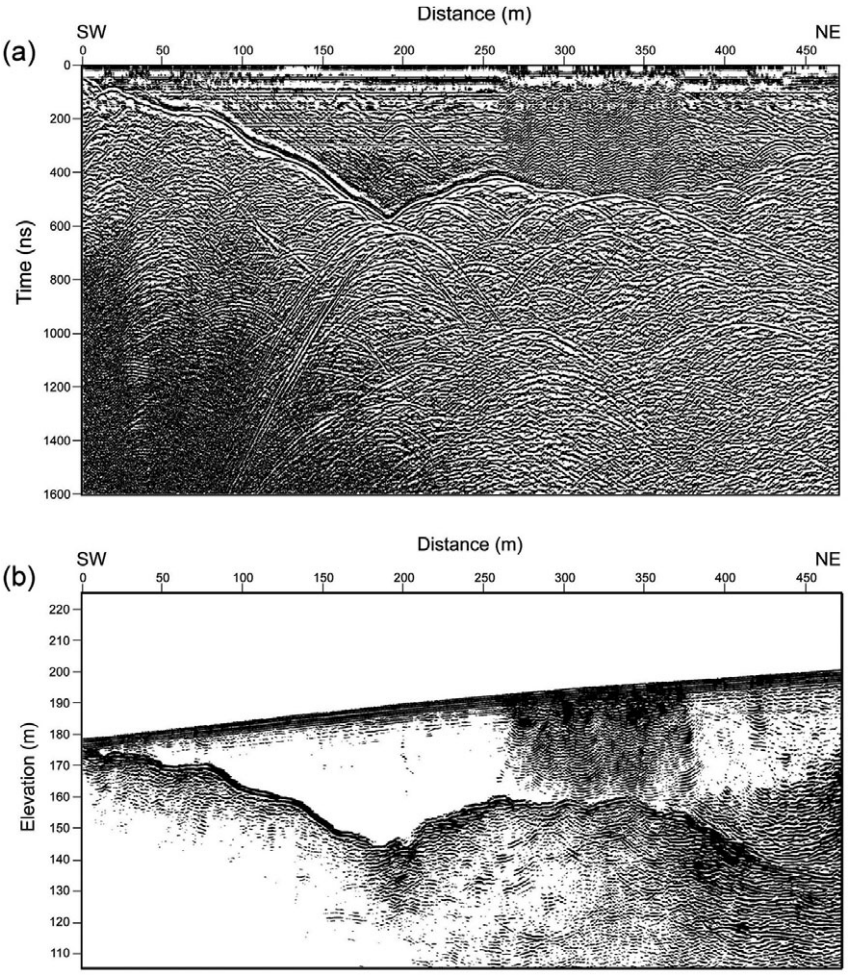

Fig. 3 Radar sections along the profile (a) before and (b) after depth migration and elevation correction. To clearly show diffractions that were used for the subsequent migration velocity analysis, automatic gain control with a 10-ns window was applied to the pre-migration data. Strong scattering noise in the ice body occurs in the distance range of 260–370 m. Migration moved dipping reflectors to their correct positions and effectively collapsed most of the diffractions.

editing, removal of DC components, bulk time shifts of 51.0 ns, geometric spreading correction and zero-phase 25–80-MHz bandpass filtering. Strong radar signatures, directly transmitted through the air and along the air–ice interface, were attenuated by subtracting a calculated mean trace from all traces before normal move-out (NMO) correction for the source–receiver offset of 4.0 m (Fig. 3a). Signature deconvolution using reflection signals (Fig. 4a) increased the vertical resolution prior to velocity analysis. Constant velocity migration in the frequency–wavenumber (F–K) domain used the Stolt (1978) algorithm to collapse and analyse 112 diffraction events. Migration velocities in the range of 100–188 m μs^{-1} at a 1 m μs^{-1} interval were examined. The F–K migration technique is superior to the most common procedure for measuring radar velocity: the common midpoint (CMP) method (Yilmaz 2001; Murray et al. 2000), where the velocity gradients and the maximum offset to depth ratio are not small, and planar reflections are rare (Bradford & Harper 2005). A smoothly varying migration velocity was then derived as a function of time and profile distance from the analysis of individual diffractions. From the smoothed migration velocity function, interval velocities were derived using Dix's equation (Dix 1955) before application of 2D depth migration to the deconvolved data, with a depth increment of 0.1 m and a maximum dip of 65°. The variable velocity post-stack depth migration was based on a 45° implicit finite-difference algorithm in the frequency–space (ω–x) domain (Claerbout 1985; Yilmaz 2001).

The average migration velocity near the base of the glacier is approximately 153 m μs^{-1}. For a frequency of 50 MHz and a velocity of 153 m μs^{-1}, the horizontal resolution after migration with an aperture width of 200 m is approximately 1.2 m at a 25-m depth, assuming the far-field and plane wave approximation (Chen & Schuster 1999). After elevation correction, the migration section shows that dipping reflectors were moved to their correct positions and most diffractions were effectively collapsed,

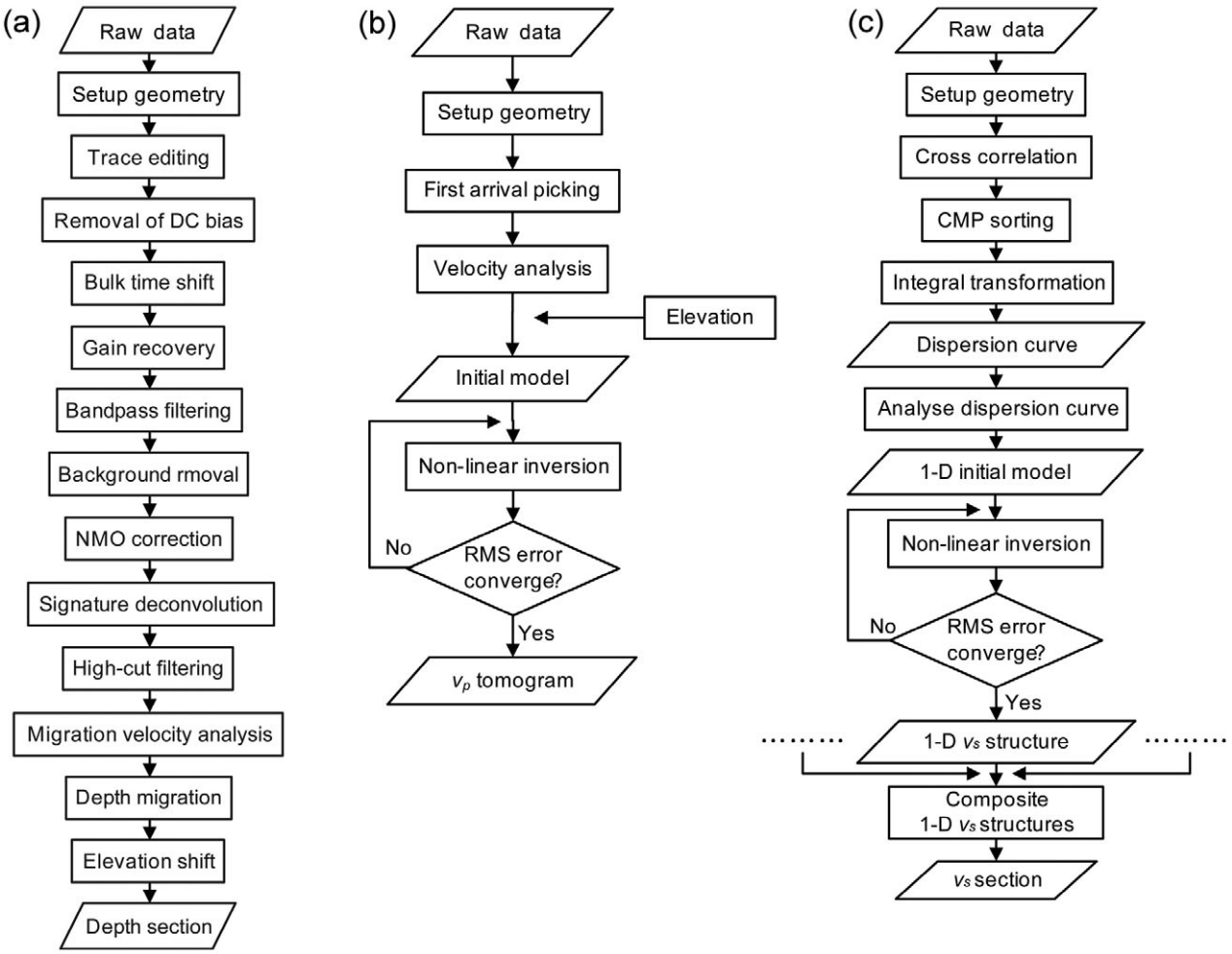

Fig. 4 Flowcharts illustrating the processing sequences for (a) ground-towed ground-penetrating radar data, (b) P-wave travel times and (c) S-wave velocity inversion from Rayleigh wave dispersions.

and the horizontal resolution was thereby improved (Fig. 3b).

P-wave processing and travel-time tomography

First the P-wave data were reformatted into the SEG-Y format (one of several standard formats developed by the Society of Exploration Geophysicists), and then the source–receiver geometry was determined (Fig. 4b). First arrival times of direct and refracted events (Fig. 5) were then picked and used for inversion by the simultaneous iterative reconstruction technique (SIRT) of Lo & Inderwiesen (1994) to yield a velocity tomogram (Fig. 6). The tomographic inversion required an initial model. For this, we used a two-layer model and derived the ice/basement boundary from the radar image (Fig. 3b). For initial model velocities of the ice and basement, we used 3550 and 4500 m s^{-1}, respectively, which we derived as approximate averages of apparent velocities of near- and far-offset quasi-linear refraction events in the travel-time curves (Fig. 5).

The inversions used 30 layers of constant-velocity cells with 10-m widths equal to the interval between receiver stations. With increasing depth, the cell height increases from about 0.5 to 2.3 m. Grid points near the base of the glacier were vertically adjusted to minimize any misfit between the cell boundary and the radar basement. Accordingly, location error ranges in the vertical and horizontal directions are nominally less than 1.0 and 5.0 m, respectively. Modelling based on Huygens' principle (Saito 1989) automatically selected the shortest travel time paths, comprising straight-line segments between nodes on perimeters of the rectangular cells, with 20 nodes on each cell edge. After three iterations, the root-mean-square (RMS) errors in the modelled travel times converged to less than 1.0 ms. Except in the

vicinity of interfaces between layers of greatly different velocity, the velocity error in each cell is probably less than 10%. Cell dimensions, and the smoothing necessary to ensure computational stability, limit the resolution by seismic inversion. Nevertheless, the resultant velocity tomogram and computed ray paths (Fig. 6) image the base of the glacier at depths in excess of 48 m, and confirm the interpretation of the glacier's base in the depth-migrated GPR section (Fig. 3b). The P-wave velocity of 4000 m s^{-1} defines the radar basement with an error not exceeding a few metres.

Inversion of Rayleigh wave dispersion curves

To obtain shear wave velocities with higher spatial resolutions, we used the common midpoint cross-correlation analysis (CMPCC) method (Hayashi & Suzuki 2004), which is modified from the multi-channel analysis of surface waves (MASW) technique (Park et al. 1999). To use the CMPCC method, every pair of traces in each shot gather was cross-correlated before being sorted into CMP gathers. In each CMP gather, the equally spaced traces were stacked in the time domain to yield CMP cross-correlation gathers. To image dispersion curves in the phase velocity versus frequency domain, phases of the cross-correlated data were shifted and stacked in the frequency domain, as described in Park et al. (1999). The resultant dispersion image near the south-west end of the profile (Fig. 7a) shows that phase velocity increases from 1706 m s^{-1} at 300 Hz to 2400 m s^{-1} at 48 Hz. Near the profile distance of 365 m, where the ice is much thicker, the phase velocity is 1683 m s^{-1} at 300 Hz and 1800 m s^{-1} at 25 Hz (Fig. 7b). Best-estimate dispersion curves (Fig. 7c) were picked at the peaks of the cross-correlation plots.

At each CMP location, 1D V_S structures were derived by a nonlinear least squares inversion of the dispersion curve using a stack of homogeneous layers, and the Thomson–Haskell method (Thomson 1950; Haskell 1953), to compute phase velocities. Because the effects of V_S on the phase velocity of Rayleigh waves dominate the effects of V_P and ρ (Xia et al. 1999), the empirical relationships of V_P/V_S and ρ/V_S were used in inversions. For these inversions, 20 layers of cells of 2.0 m in height were used; therefore, the location error ranges in the vertical and horizontal directions are 1.0 and 20.0 m, respectively, prior to the subsequent smoothing. The 2D V_S section (Fig. 8b) was obtained by spatially averaging adjacent 1D models with a 60-m, three-point [(1, 1, 1)/3] smoothing filter. The displayed velocities are for depths of 24 m or less. Reliable velocity estimates can be derived only for these depths, which are less than or approximately equal to half of the longest wavelengths useful to inversion. Two-dimensional interpolation by kriging (Deutsch & Journel 1992) preceded the contouring of V_P and V_S (Fig. 8a, b), and the computation of the derived elastic constants at more than 3000 nodes (Fig. 8c, d).

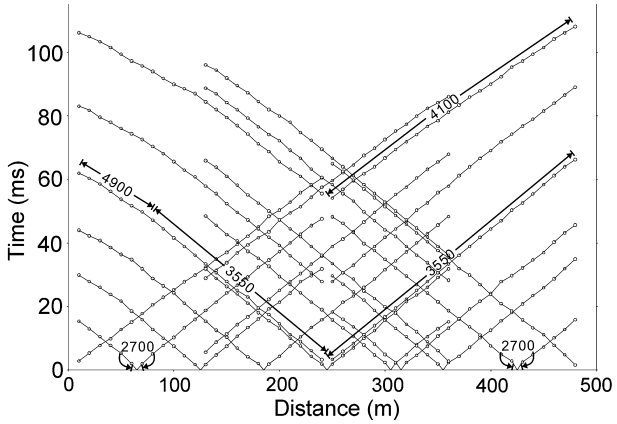

Fig. 5 Travel time curves showing first-arrival picks along the seismic profile. Tomography was used to identify the arrivals resulting from refraction through the bedrock and the arrivals resulting from travel paths confined to the ice layer. Apparent velocities for some direct arrivals and refraction events are indicated in m s^{-1}. The horizontal axis shows the distance from the south-west end of the profile. Each record used 24 geophones at intervals of 10 m.

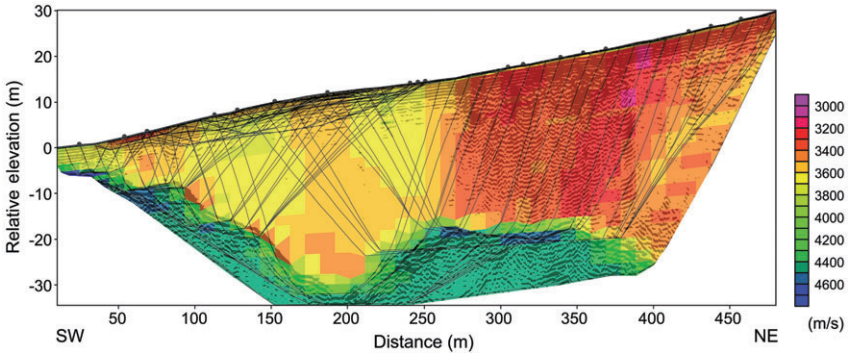

Fig. 6 P-wave velocity tomogram for the seismic profile superimposed on the ground-penetrating radar depth-migrated image (Fig. 3b). A distinctive low-velocity region is imaged in the profile distances between 260 and 380 m, where the ice is densely fractured. The 21 shot locations are indicated by dots on the ice surface. Solid lines indicate the modelled raypaths emanating from these shots.

Errors in estimating the shear-wave velocities depend on many factors, including frequency range, number of recording channels, source offset, spatial sampling interval, spread length, complexity of subsurface structures, and number of iterations. Even in a geologically more complex area along the Fraser River in Vancouver, Canada, the maximum difference between the V_S inverted from Rayleigh waves and borehole-measured V_S in eight wells was less than 15% (Xia et al. 2002). Similar differences in V_S values of less than 10% were determined for depths of less than 50 m in Santa Clara Valley, California, USA (Stephenson et al. 2005). However, near the south-west end of our profile, the low common midpoint fold and the narrow offset range reduce the resolution of the dispersion curves, which may cause greater errors in computing V_S.

To roughly estimate errors in V_S for the present study in which ice cores were not available, "offset" dispersion curves were set at the half-width of the main lobe of the cross-correlation functions for phase velocities below and above those of the best-estimate dispersion curves (Fig. 5c). Those offset dispersion curves were then inverted to obtain lower and upper offset estimates of V_S, respectively (Fig. 9). Near the south-west end of the profile, where the basement is shallow, the resultant values of V_S at the basement boundary 12.5 m deep differed from the best-estimate value by −395 and 44 m s^{-1}, respectively (Fig. 9a). At a depth of 1.5 m, these differences were −40 and 60 m s^{-1}, respectively. Near the profile distance of 365 m where the ice is relatively thick, the differences in V_S at a depth of 24.5 m were −270 and 188 m s^{-1} (Fig. 9b). At a depth of 1.5 m, these differences were −39 and 23 m s^{-1}, respectively.

Determination of density and elastic parameters

Because glacial ice is nonmagnetic and is generally of very low conductivity, its relative permittivity, ε_S, is directly derived from the radar velocity (Reynolds 1997). The cube root of the dielectric permittivity of an ice–air–water mixture is a volume-weighted average of the cube roots of the dielectric permittivity of the media components (Looyenga 1965):

$$\varepsilon_s = \left[\varepsilon_i^{1/3}(1-P) + W\varepsilon_w^{1/3} + P - W\right]^3, \quad (1)$$

where the relative permittivity of air is unity; ε_i and ε_w are the relative permittivities of solid ice and water; and P and W are the porosity and water content of the ice, respectively. The relative permittivities of ice and water are

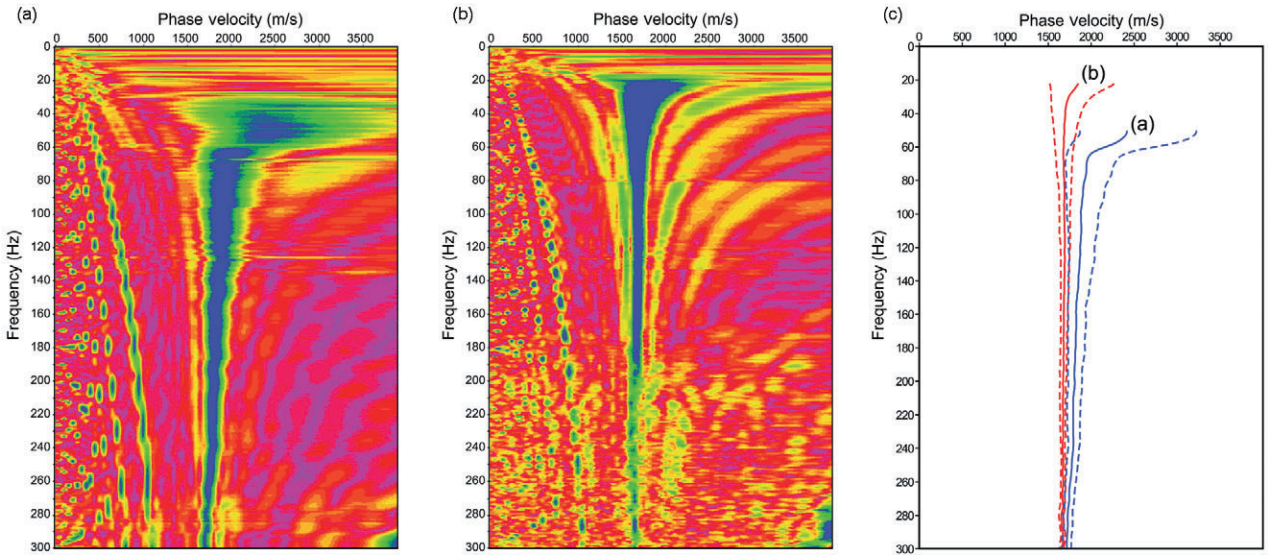

Fig. 7 Phase velocity spectra of Rayleigh waves: (a) near the south-west end of the profile, where the basement is shallow; (b) near the profile distance of 365 m, where the ice is relatively thick; and (c) the corresponding best-estimate (solid) and "offset" (dashed) dispersion curves.

Fig. 8 (a) P-wave velocities (V_P) and (b) S-wave velocities (V_S) derived from one-dimensional inversions of Rayleigh wave dispersion curves; (c) k and (d) μ sections superimposed on the depth-migrated ground-penetrating radar image section. The distinctive low V_P in (a) and k in (c) are imaged in the profile distances between 260 and 380 m, where the ice is densely fractured. The lowest V_s (b) and μ (d) values occurring at depths of about 20 m may indicate that warmer ice at this depth underlies relatively cold ice. The low V_s (b) and μ (d) values near the surface ice are probably caused by superficial melting during the summer season.

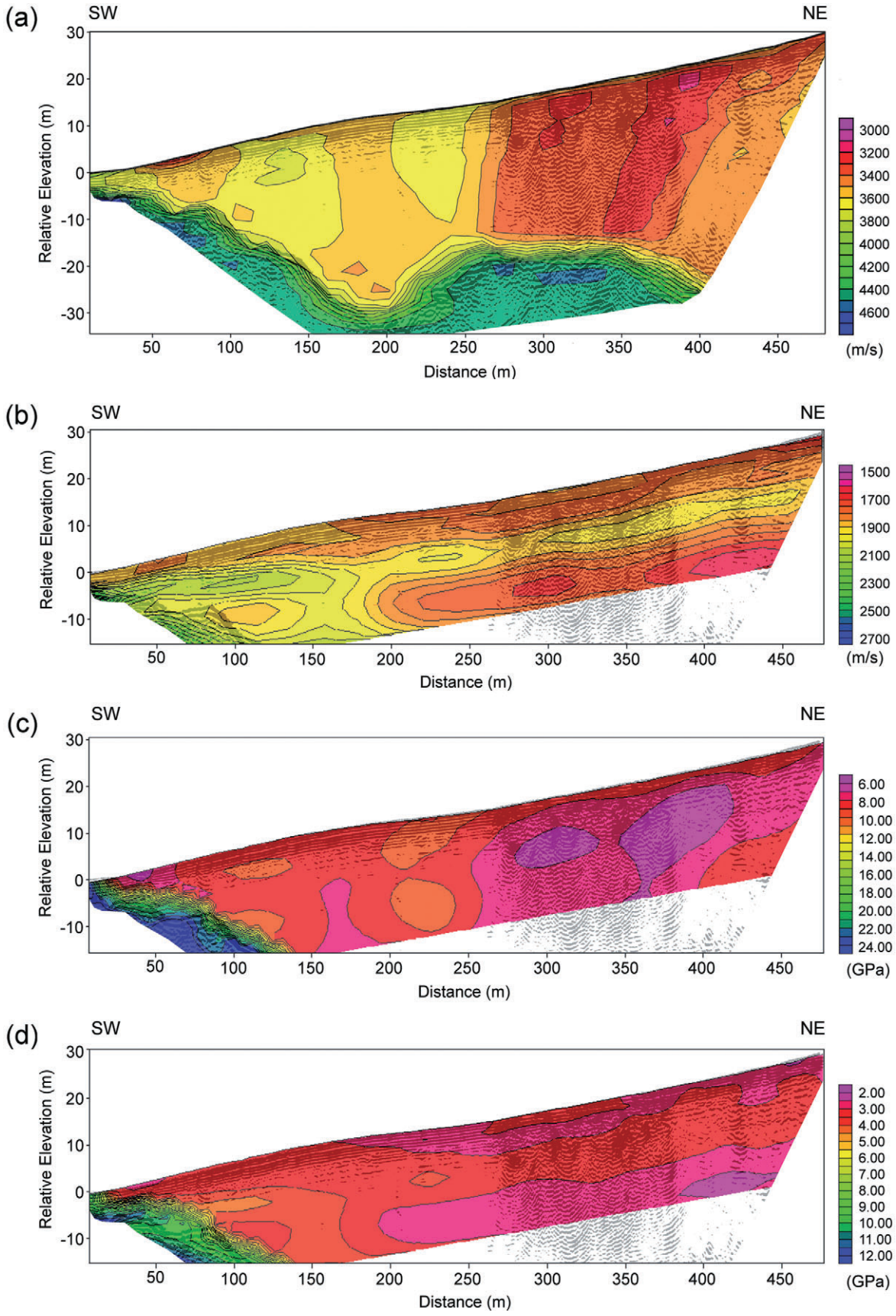
(a)
SW
NE
Relative Elevation (m)
30
20
10
0
-10
-20
-30
50
100
150
200
250
300
350
400
450
Distance (m)
3000
3200
3400
3600
3800
4000
4200
4400
4600
(m/s)
(b)
SW
NE
Relative Elevation (m)
30
20
10
0
-10
50
100
150
200
250
300
350
400
450
Distance (m)
1500
1700
1900
2100
2300
2500
2700
(m/s)
(c)
SW
NE
Relative Elevation (m)
30
20
10
0
-10
50
100
150
200
250
300
350
400
450
Distance (m)
6.00
8.00
10.00
12.00
14.00
16.00
18.00
20.00
22.00
24.00
(GPa)
(d)
SW
NE
Relative Elevation (m)
30
20
10
0
-10
50
100
150
200
250
300
350
400
450
Distance (m)
2.00
3.00
4.00
5.00
6.00
7.00
8.00
9.00
10.00
11.00
12.00
(GPa)

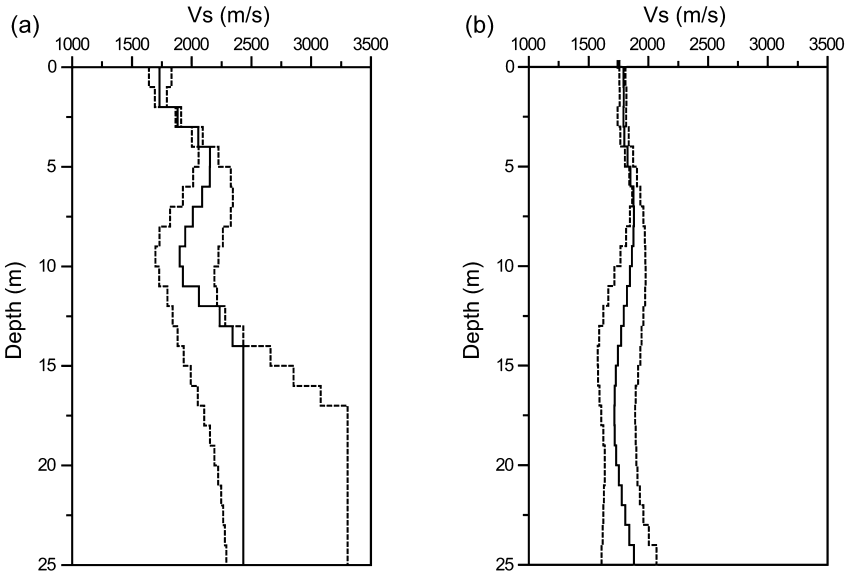

Fig. 9 S-wave velocities (V_s) derived from one-dimensional inversions of the best-estimate and "offset" Rayleigh wave dispersion curves in Fig. 7c: (a) near the south-west end of the profile where the basement is shallow, and (b) near the profile distance of 365 m where the ice is relatively thick.

3.19 ± 0.04 at the temperature of 0°C (Mätzler & Wegmüller 1987) and 86.0 in the radar frequency range (Smith & Evans 1972), respectively. Macheret & Glazovsky (2000) presented plots of radar velocity as a function of water content using Eqn. 1 with an assumed air content of zero. For a given permittivity, this case corresponds to the minimum water content and porosity. Generally, however, air bubbles in glacier ice can have a significant impact on radar velocity and on subsequent estimates of water content (West et al. 2007; Bradford et al. 2009).

Migration velocity analysis (Yilmaz 2001) of 57 diffractions within the glacial ice or at its base (Fig. 4a) yielded velocities between 141 and 169 m μs^{-1}, with an estimate of the mean velocity of 153 m μs^{-1}. Effects of layering and other inhomogeneity, including edge diffractors that are not perpendicular to the line of profile, can result in migration velocities that are higher than vertical average radar velocities. However, corrections for such effects are not available for these data in a single profile with discontinuous or poorly defined intra-ice reflectors. Bias may also result from a tendency for diffractions to occur in areas that are not characteristic of the average water content of the glacier. Although systematic variations of ice velocities as functions of depth and position along the profile are not entirely separable from measurement errors, the mean velocity, as determined by migration velocity analysis, may be representative of glacial ice. For a velocity of 153 m μs^{-1} and $\varepsilon_i = 3.19$, the estimated water content is 3.2% if no air is present. Considering, however, that measurement errors for the velocity may be on the order of ±5 m μs^{-1}, we compute a range of water content that would correspond to the mean velocity. For a velocity of 153 ± 5 m μs^{-1} and $\varepsilon_i = 3.19 \pm 0.04$, the estimated water content without air in any pores is between 1.9 and 4.6%. Although the ice may be wet, air can remain in pore spaces that are closed. For pore spaces containing between zero and 10% air ($W = 0.95 \pm 0.05\,P$) and $\varepsilon_i = 3.19 \pm 0.04$, the estimated water content would be between 1.9 and 4.7%. The exposed ice beneath our GPR profile was wet during the summer of 2006, and we assume that the air content was relatively small.

Larger values for water content are derived from the seismic P-wave velocities using the well-known time-average equation (Wyllie et al. 1956):

$$1/V_{Pb} = (1-P)/V_{Pi} + P/V_{Pw}, \quad (2)$$

where V_{Pb}, V_{Pi}, and V_{Pw} are P-wave velocities for porous ice, pure ice and water, respectively. The P-wave velocities of pure ice and water at 0°C are 3750 (Hausmann et al. 2007) and 1435 m s^{-1}, respectively. For the average velocity of 3466 m s^{-1} (Table 1), a porosity of 5.1% is obtained using Eqn. 2. Porosities of 7.5 and 4.0% are computed in the densely fractured zone between profile distances of 260 and 380 m, and the rest of the area, respectively.

The bulk density of the water–ice mixture, ρ_a, is:

$$\rho_a = \rho_i(1-W) + \rho_w W, \quad (3)$$

where ρ_i and ρ_w are the densities of solid ice and water, respectively. For ρ_i =916 kg m^{-3} and ρ_w = 1000 kg m^{-3}, the bulk density of the wet ice, ρ_a, would be 919 and 920 kg m^{-3} for $W = 3.2\%$ (derived from radar velocities) and 5.1% (derived from V_p), respectively. The

Table 1 Seismic velocities and computed elastic constants for the ice and the basement.

	Ice							
	Sparsely fractured		Densely fractured		Total		Basement	
	Range	Avg.	Range	Avg.	Range	Avg.	Range	Avg.
V_P (m s^{-1})	3208–3738	3524	3199–3595	3344	3199–3738	3466	3485–4512	3999
V_S (m s^{-1})	1570–2101	1857	1669–1915	1802	1570–2101	1839	1735–2689	2133
k (MPa)	5029–8453	7233	4980–7938	6304	4980–8453	6925	14976–38209	27129
μ (MPa)	2267–4059	3182	2562–3374	2992	2267–4059	3119	7501–25281	11518

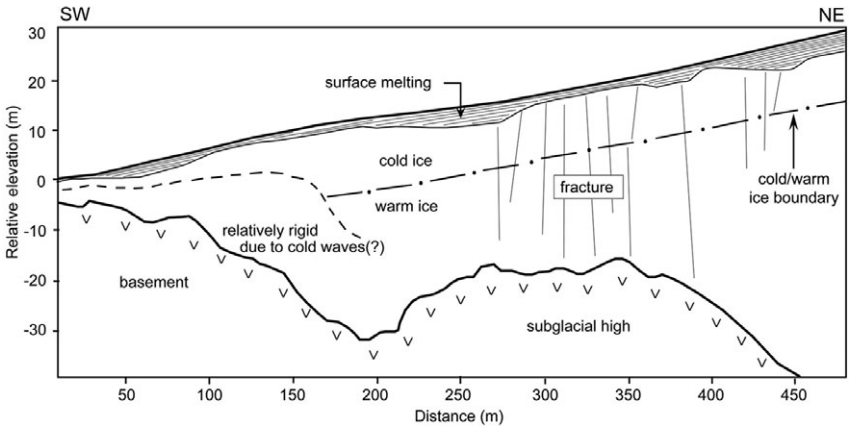

Fig. 10 Glaciological interpretation of the seismic and radar profiles in an ablation zone of Fourcade Glacier. The datum is 179 m a.s.l.

corresponding densities are thus significantly greater than the density of 830 kg m^{-3} obtained from the direct measurement of relatively dry ice below a 35-m-thick firn layer in the ice cap of KGI at a level of 690 m (Simões et al. 2004; Fig. 1). The estimated density of the glacier bed, 2520 kg m^{-3}, was derived from the average V_p of 4365 m s^{-1}, assuming that $\rho = cV_p^{0.25}$ and $c = 310$ kg m$^{-3.25}$ s$^{0.25}$ (Gardner et al. 1974).

At the frequencies of seismic waves, dispersion resulting from the viscoelasticity of ice is generally negligible. For isotropic media, the bulk modulus of incompressibility (k) and the rigidity (μ) are related to V_P, V_S and ρ as follows:

$$k = \rho\left(V_P^2 - \frac{4}{3}V_S^2\right), \quad (4)$$

and

$$\mu = \rho V_S^2. \quad (5)$$

Values for k (Fig. 8c) and μ (Fig. 8d) were computed at each grid point using Eqns. 4 and 5, the estimated velocities V_P (Fig. 6) and V_S (Fig. 8b), and the estimated densities of 920 and 2520 kg m^{-3} for the ice body and the glacier bed, respectively.

Results and discussion

The V_P tomogram (Fig. 6) shows ice velocities between 3199 and 3738 m s^{-1} (Table 1). At profile distances of 260–380 m (Fig. 8a), the interpreted velocity above the subglacier high is roughly 5% less than the velocity south-east of this high. Fractures and variations of porosity (water content) in the polythermal glacier can yield large changes in V_P. Subvertical alignments of diffraction apices in the GPR image may indicate the presence of fractures and increased water content above the subglacier high (Fig. 10), which would be consistent with the apparent decrease of seismic velocities in this region.

Benjumea & Teixidó (2001) measured a V_S of 1800 m s^{-1} on Johnsons glacier on the Livingston Island, SSIs. In our profile of Fourcade Glacier, the derived S-wave velocity at a depth of ca. 20 m is also approximately 1800 m s^{-1} above the subglacial high (Fig. 8b). At this depth the velocity above the high is roughly 3% less than the velocity above the subglacial low to the south-east. The lower V_s velocities thus roughly correlate with the increased radar diffraction noise above the subglacial high, and V_S may be lowered by the presence of fractures in this region (Fig. 10). For a fixed density, a 3% decrease in V_S corresponds to a decrease in rigidity of 6%. Such

changes are near the limits of resolution for the methods used here.

North-east of the 200-m location, the highest shear wave velocities of the ice occur at depths of 8 to 10 m. The velocity decreases both upward and downward from this central high (Fig. 8b). Such layered structure is characteristic of polythermal glaciers. A similar variation of V_S derived from borehole measurements has been observed in a valley glacier in Spitsbergen (Ødegård et al. 1992). This variation of V_S may correspond to changes in water content of the polythermal Fourcade Glacier. The seismic profile lies in an ablation zone below the ELA of 270 m altitude. Along the profile, we interpret that less rigid and warm ice with slower shear-wave velocities are overlain by more rigid cold ice of 10–15 m thickness that is in turn overlain by ice that was partially melted during the austral summer of 2006 (Fig. 10). The surface layer of the glacier is at or near the pressure melting point (Bintanja 1995). This layer created strong scattering noise in the near-surface GPR data (Fig. 3). North-east of the 200-m location, the highest shear wave velocity of the ice corresponds to rigidity, μ, of 3.7 GPa, which is slightly lower than measured values of 3.8–3.9 GPa near the melting point (Gold 1958; Prensky 1995). Since V_S^2 depends linearly on μ and a constant density for the ice has been assumed, the contoured μ and V_S (Fig. 8b, d) show similar features. Adjacent to bedrock outcrops near the south-west end of the profile, V_S in excess of 2,100 m/s are indicated (Fig. 8b). These higher velocities may result from overestimation of phase velocities, low coverage in the cross-correlation data, effects of dipping layers, and decreased resolution of dispersion curves. Alternatively, however, these velocities may indicate that the ice velocity is higher here due to summer melting and winter re-freezing associated with winter cold waves (Fig. 10).

In the region between the 100- and 250-m locations, the average estimated bulk modulus, k, of the ice is approximately 8.5 GPa (Fig. 8c), which is close to the values of 8.7–8.8 GPa that were derived from laboratory measurements for ice near the melting point (Gold 1958; Prensky 1995). At the 4–14 m depth interval between the 260 and 380-m locations in the profile, the estimated values of k are significantly lower. This corresponds to the region in which we have interpreted significantly greater fracturing of the ice (Fig. 10). For a fixed density, the relative error in the estimated bulk modulus, k, depends on the relative errors in V_P and V_S and on the actual ratio V_P/V_S. For V_P/V_S determined by the average values for V_P and V_S of the ice in Table 1 (3466 m/s and 1839 m/s, respectively), overestimating V_P by 3% while underestimating V_S by 3% would overestimate k by 13%. The errors in estimating k are greater if the relative errors in V_P and V_S are of opposite signs. For a fixed density, and the same relative increases or decreases in both V_P and V_S by 3%, k would increase or decrease by 6%.

Conclusions

Synergistic interpretations of seismic P-waves, using travel-time tomography, dispersion of Rayleigh waves and GPR data in a coincident profile across a portion of the polythermal Fourcade Glacier allowed the interpretation of the glacier's configuration, its elastic properties, and such features as fractures and layering related to variations in the temperature and water content (W) of the ice. Average values of W in saturated ice, of 3.2 and 5.1%, were estimated using radar and P-wave seismic (V_P) velocities, respectively. The corresponding bulk density (ρ) estimate of 920 kg m^{-3} was, in turn, used to derive the elastic parameters of incompressibility (k) and rigidity (μ) from the seismic velocities within the ice.

Average V_P and V_S values of 3466 and 1839 m s^{-1}, respectively, for ice yield estimates for the k and μ of 6.925 and 3.119 GPa, respectively. In the ice of the densely fractured zone above the subglacial high, the average k is estimated as low as 6.9 GPa because of lower values of V_P. The V_P and V_S values are approximately 5 and 3% less than those in the ice above a subglacial valley, respectively. Rigid ice ($\mu \approx 4.0$ Gpa) in the vicinity of the outcrop near the southwest end of the profile may indicate the effects of summer melting and winter re-freezing associated with winter cold waves. Elsewhere in the profile, relatively rigid cold ice of 10–15 m in thickness is apparently indicated by higher V_S values between the partially melted top layer and deeper warm ice. A near-surface layer of cold ice overlying warmer ice at the melting point is characteristic of polythermal glaciers.

Acknowledgements

This work was supported through the Korea Science and Engineering Foundation grant R01-2007-000-20194-0 by the Ministry of Science and Technology and through grant PE07020 by the Korea Polar Research Institute under grant PE07020. We thank Dr. Jong Ik Lee, at the Korea Polar Research Institute, who supported us in many aspects for the fieldwork. We are also grateful to Dr. Moon Young Choe, the 19th commander of King Sejong station, and his overwinter crews who provided transportation and otherwise assisted in data acquisition. Finally, we are grateful to Dr. R.M. René at René Geophysics for his helpful discussions and suggestions during the progress of this work.

References

Aki K. & Richard P.G. 1980. *Quantitative seismology*. San Francisco: W.H. Freeman & Co.

Benjumea B. & Teixidó T. 2001. Seismic reflection constants on the glacial dynamics of Johnsons Glacier, Antarctica. *Journal of Applied Geophysics 44*, 31–44.

Bintanja R. 1995. Local surface energy balance of the Ecology Glacier, King George Island, Antarctica: measurements and modeling. *Antarctic Science 7*, 315–325.

Bradford J.H. & Harper J.T. 2005. Wave field migration as a tool for estimating spatially continuous radar velocity and water content in glaciers. *Geophysical Research Letters 32*, L08502, doi:10.1029/2004GL021770.

Bradford J.H., Nichols J., Mikesell T.D. & Harper J.T. 2009. Continuous profiles of electromagnetic wave theory and water content in glaciers: an example from Bench Glacier, Alaska, USA. *Annals of Glaciology 50*, 1–9.

Braun M. & Rau F. 2000. Using a multi-year data archive of ERS SAR imagery for the monitoring of firn line positions and ablation patterns on the King George Island ice cap (Antarctica). *EARSeL eProceedings 1*, 281–291.

Braun M., Simões J.C., Vogt S., Bremer U.F., Saurer H., Aquino F.E. & Ferron F.A. 2004. A new satellite image map for King George Island, Antarctica. *Pesquisa Antártica Brasileira 4*, 199–203.

Chen J. & Schuster G.T. 1999. Resolution limits of migration images. *Geophysics 64*, 1046–1053.

Claerbout J.F. 1985. *Imaging the Earth's interior*. Palo Alto: Blackwell Scientific Publications.

Curl J.E. 1980. *A glacial history of the South Shetland Islands, Antarctica. Institute of Polar Studies Report 63*. Columbus, OH: Ohio State University.

Danbom S.H. & Domenico S.N. 1986. *Shear-wave exploration*. Tulsa: Society of Exploration Geophysicists.

Deutsch C.V. & Journel A.G. 1992. *GSLIB: Geostatistical Software Library and user's guide*. Cambridge: Oxford University Press.

Dix C.H. 1955. Seismic velocities from surface measurements. *Geophysics 34*, 180–195.

Dorman J. & Ewing M. 1962. Numerical inversion of seismic surface wave dispersion data and crust-mantle structure in the New York–Pennsylvania area. *Journal of Geophysical Research 67*, 5227–5241.

Duval P. 1977. The role of water content on the creep rate of polycrystalline ice. *IAHS Publication Series 118*, 29–33.

Ferron F.A., Simões J.C., Aquino F.E. & Setzer A.W. 2004. Air temperature time series for King George Island, Antarctica. *Pesquisa Antártica Brasileira 4*, 155–169.

Fountain A.G. & Walder J.S. 1998. Water flow through temperate glaciers. *Reviews of Geophysics 36*, 299–329.

Furbish D.J. & Andrews J.T. 1984. The use of hypsometry to indicated long-term stability and response of valley glaciers to changes in mass transfer. *Journal of Glaciology 30*, 199–211.

Gardner G.H.F., Gardner L.W. & Gregory A.R. 1974. Formation velocity and density—the diagnostic basics for stratigraphic traps. *Geophysics 39*, 770–780.

Glen J.W. & Paren J.G. 1975. The electrical properties of snow and ice. *Journal of Glaciology 15*, 15–38.

Gold L.W. 1958. Some observations on the dependence strain on stress for ice. *Canadian Journal of Physics 36*, 1265–1275.

Haskell N.A. 1953. The dispersion of surface waves in multilayered media. *Bulletin of the Seismological Society of America 43*, 17–34.

Hausmann H., Krainer K., Brückl E. & Mostler W. 2007. Internal structure and ice content of Reichenkar rock glacier (Stubai Alps, Austria) accessed by geophysical investigations. *Permafrost and Periglacial Processes 18*, 351–367.

Hayashi K. & Suzuki H. 2004. CMP cross-correlation analysis of multi-channel surface-wave data. *Exploration Geophysics 35*, 7–13.

Jeon S.H. & Suh G.T. 2006. Atmospheric science. In S.M. Hong (ed.): *Overwintering report of the 18th Korea Antarctic Research Program at King Sejong Station (Dec. 2004–Feb. 2006)*. Ansan: Korea Polar Research Institute.

King J.C. 1994. Recent climate variability in the vicinity of the Antarctic Peninsula. *International Journal of Climatology 14*, 357–369.

Lee J.I., Hur S.D., Yoo C.M., Yeo J.P., Kim H., Hwang J., Choe M.Y., Nam S.H., Kim Y., Park B.-K., Zheng X. & López-Martínez J. 2002. *Geologic map of Barton and Weaver peninsulas, King George Island, Antarctica (1 : 10,000)*. Ansan: Korea Ocean Research and Development Institute.

Lo T. & Inderwiesen P. 1994. *Fundamentals of seismic tomography*. Tulsa: Society of Exploration Geophysicists.

Looyenga H. 1965. Dielectric constants of heterogeneous mixture. *Physika 31*, 401–406.

Macheret Y.Y. & Glazovsky A.F. 2000. Estimation of absolute water content in Spitsbergen glaciers from radar sounding data. *Polar Research 19*, 205–216.

Mätzler C. & Wegmüller U. 1987. Dielectric properties of fresh-water ice at microwave frequencies. *Journal of Physics D: Applied Physics 20*, 1623–1630.

Moll A., Braun M. & Lluberas A. 2006. Determination of glacier velocities on King George Island (Antarctica) by DInSAR. In H. Lacoste & L. Ouwehand (eds.): *Fringe 2005 Workshop, proceedings of the conference held 28 November–2 December, 2005 in Frascati, Italy. ESA SP-610*. On CD-ROM. European Space Agency.

Murray T., Booth A. & Rippin D.M. 2007. Water-content of glacier-ice: limitations on estimates from velocity analysis of surface ground-penetrating radar surveys. *Journal of Environmental and Engineering Geophysics 12*, 87–99.

Murray T., Stuart G.W., Fry M., Gamble N.H. & Crabtree M.D. 2000. Englacial water distribution in a temperate glacier from surface and borehole radar velocity analysis. *Journal of Glaciology 46*, 389–398.

Ødegård B.S., Hamran S.-E., Bø P.H., Etzelmüller B.E., Vatne G. & Sollid J.L. 1992. Thermal regime of a valley

glacier, Erikbreen, northern Spitsbergen. *Polar Research 11*, 69–79.

Park C.B., Miller R.D. & Xia J. 1999. Multichannel analysis of surface waves. *Geophysics 64*, 800–808.

Poisson S.-D. 1828. Mémoire sur l'équilibre et le mouvement des corps élastiques. (The equilibrium and movement of elastic bodies.) *Mémoires de l'Académie Royale des Sciences de l'Institut de France 8*, 357–570.

Reynolds J.M. 1997. *An introduction to applied and environmental geophysics*. Chichester: John Wiley & Sons.

Prensky S.E. 1995. A review of gas hydrates and formation evaluation of hydrate-bearing reservoirs (paper GGG). Paper presented at the Society of Petrophysicists & Well Log Analysts Annual Logging Symposium, New Orleans, LA, USA, 1995 meeting of the Society of Professional Well Log Analysts, 16–19 June, Paris, France.

Rix G.J. & Leipski E.A. 1991. Accuracy and resolution of surface wave inversion. In S.K. Bhatia & G.W. Blaney (eds.): *Recent advances in instrumentation, data acquisition and testing in soil dynamics*. Pp. 17–32. Orlando, FL: American Society of Civil Engineers.

Saito H. 1989. Traveltimes and raypaths of first arrival seismic waves: computation method based on Huygens' principle. In: *Expanded abstracts, 59th Annual International SEG Meeting*. Pp. 244–247. Tulsa: Society of Exploration Geophysicists.

Sheriff R.E. 2002. *Encyclopedic dictionary of applied geophysics*. Tulsa: Society of Exploration Geophysicists.

Simões J.C., Bremer U.F., Aquino F.E. & Ferron F.A. 1999. Morphology and variations of glacial drainage basins in the King George Island ice field, Antarctica. *Annals of Glaciology 29*, 220–224.

Simões J.C., Ferron F.A., Bernardo R.T., Aristarain A.J., Stievenard M., Pouchet M. & Delmas R.J. 2004. Ice core study from King George Island, South Shetlands, Antarctica. *Pesquisa Antártica Brasileira 4*, 9–23.

Smith B. & Evans S. 1972. Radio echo sounding absorption and scattering by water inclusion and ice lenses. *Journal of Glaciology 11*, 133–146.

Smith R.C., Stammerjohn S.E. & Baker K.S. 1996. Surface air temperature variations in the western Antarctic Peninsula region. *Antarctic Research Series 70*, 105–121.

Stephenson W.J., Louie J.N., Pullammanappallil S., Williams R.A. & Odum J.K. 2005. Blind shear-wave velocity comparison of ReMi and MASW results with boreholes to 200 m in Santa Clara Valley: implications for earthquake ground-motion assessment. *Bulletin of the Seismological Society of America 95*, 2506–2516.

Stolt R.H. 1978. Migration by Fourier transform. *Geophysics 4*, 23–48.

Thomson W.T. 1950. Transmission of elastic waves through a stratified solid. *Journal of Applied Physics 21*, 89–93.

West L.J., Rippin D.M., Murray T., Mader H.M. & Hubbard B. 2007. Dielectric permittivity measurements on ice cores: implementations for interpretation of radar to yield glacial unfrozen water content. *Journal of Environmental and Engineering Geophysics 12*, 37–45.

Wyllie M.R.J., Gregory A.R. & Gardner L.W. 1956. Elastic wave velocities in heterogeneous and porous media. *Geophysics 21*, 41–70.

Xia J., Miller R.D. & Park C.B. 1999. Estimation of near-surface shear-wave velocity by inversion of Rayleigh waves. *Geophysics 64*, 691–700.

Xia J., Miller R.D., Park C.B., Hunter J.A., Harris J.B. & Ivanov J. 2002. Comparing shear-wave velocity profiles inverted from multichannel surface wave with borehole measurements. *Soil Dynamics and Earthquake Engineering 22*, 181–190.

Yilmaz Ö. 2001. *Seismic data analysis: processing, inversion and interpretation of seismic data*. Tulsa: Society of Exploration Geophysicists.

Zwally H.J., Abdalati W., Herring T., Larson K., Saba J. & Steffen K. 2002. Surface melt-induced acceleration of Greenland ice-sheet flow. *Science 297*, 218–222.